Research Article Vol. 30, No. 7 / 28 Mar 2022 / *Optics Express* 10942

Optics EXPRESS

Simultaneous measurement of axial strain and lateral stress based on cascaded interference structure

YUJIAN LI,[1] ZHENGYONG LIU,[2,3] YIFAN LIU,[1] AND CHANGYUAN YU[1,*]

[1] *Department of Electronic and Information Engineering, The Hong Kong Polytechnic University, Hong Kong, China*
[2] *Guangdong Provincial Key Laboratory of Optoelectronic Information Processing Chips and Systems, School of Electronics and Information Technology, Sun Yat-sen University, Guangzhou 510275, China*
[3] *Southern Marine Science and Engineering Guangdong Laboratory (Zhuhai), Zhuhai 519000, China*
[*] *changyuan.yu@polyu.edu.hk*

Abstract: To solve the cross-sensitivity problem in the dual-parameter optical fiber system, a new type of sensor based on cascaded interference structure is proposed without cross-sensitivity. The design consists of a Michelson interferometer and a Sagnac interferometer based on a high-birefringence suspended core fiber segment. After calculating by the analogous Fast Fourier Transformation (FFT) and filtering by FFT filter, the spectrum of the sensor responds linearly to the change of axial strain and lateral stress. The sensitivity to lateral stress is 3.13 nm/(kPa) in the range from 0 to 1200 Pa and the axial strain is 1.846e^{-4} (nm·με)$^{-1}$ from 0 to 4000 με. The capability of the proposed sensor for dual-parameter sensing is also experimentally demonstrated. The precision rate for dual-parameter sensing is as high as 66.7%, reflecting the sensor's usability for simultaneous measurement of axial strain and lateral stress.

1. Introduction

Ever since the optical fiber sensor comes out, it has presented unique and exciting properties, such as anti-electromagnetic interference, high response speed, remote sensing capability, and so on [1–5]. All of the advantages make its popularity in many application fields, such as boundary protection systems in the military area, large building health monitoring systems in the engineering field, and vital signs data acquisition systems in medical fields [6–8].

With the demand changing in different fields, the research focus on optical fiber sensors has gradually shifted from single parameter sensing to dual or multi parameters sensing. Up to now the structures designed could be classified into two categories. The first one is realizing the dual-parameter sensing based on the different characteristics of a single structure. The principle is that the different features of the sensor can respond to specific environmental variations. For example, an inline Mach-Zehnder interferometer (MZI) could be used to simultaneously measure strain and temperature because of the sensitivity difference between different interference dips [9]. Refractive index and strain could be measured at the same time by the fiber Bragg grating (FBG) because the period of the grating is sensitive to the axial strain change while the mode effective refractive index is sensitive to the external environment refractive index fluctuation [10]. However, this type of sensor has great cross-sensitivity because the same characteristic of the sensor may not only respond to just one environmental parameter [11–15]. Another way to achieve dual-parameter sensing is to combine different sensing structures. For example, FBG is combined with photonic crystal fiber (PCF) for simultaneous measurement of magnetic field and temperature [16], FBG is combined with Fabry-Perot (FP) to achieve measurement of the temperature and gas pressure at the same time, two Sagnac interferometers (SI) were cascaded

#452783 https://doi.org/10.1364/OE.452783
Journal © 2022 Received 31 Dec 2021; revised 18 Feb 2022; accepted 21 Feb 2022; published 16 Mar 2022

Corrected 21 March 2022

together to simultaneously measure the temperature and strain [17]. However, this type of sensor has great cross-sensitivity and high insert loss introduced by the mismatch between different structures. In addition, the demodulation method for most dual-parameter sensors usually is calculating the cross-sensitivity matrix [18–20]. The effectiveness of the cross-sensitivity matrix is related to the sensitivity difference [21]. The greater the difference will give rise to better performance of the sensor. Thus, it is crucial for a dual-parameters sensor to reduce measurement errors caused by cross-sensitivity when working in complex environments.

In this paper, a dual-parameters sensor based on a cascaded interference structure is designed and fabricated to simultaneously measure axial strain and lateral stress without crosstalk. The sensor consists of one Michelson Interferometer (MI) and one SI. Through low-power fusion splicing process, the MI and SI can share the same optical coupler which means the MI exists in the SI loop. Experimental results show that the spectrum of the MI part is sensitive to the axial strain with a sensitivity of $1.846\mathrm{e}^{-4}$ $(\mathrm{nm}\cdot\mu\varepsilon)^{-1}$ while the spectrum of the SI part is sensitive to the lateral stress with a sensitivity of 3.13 nm/(kPa). Since the axial strain and lateral stress sensing are realized by the different parts of the sensor, there is no cross-sensitivity between the two parts which ensures the sensor's accuracy for practical sensing.

2. Fabrication

Figure 1(a) is the structural representation of the high-birefringence suspended core fiber (HB-SCF) and Fig. 1(b) is the cross-section view of the HB-SCF observed under a scanning electron microscope. The cladding diameter of HB-SCF is 125 μm, which is the same as the standard single-mode fiber (SMF). There are six large air holes around the elliptical core, of which the long axis size is about 8 μm and the short axis size is approximately 4 μm. The size of the air holes is about 22 μm by 27 μm. The fabrication process and optical characteristics of the HB-SCF have been researched and published by Zhengyong Liu *et al*. [22]. The size difference between two axes of the fiber core offers a large group modal birefringence, which value is about -4.75×10^{-4} at 1550 nm. Thus, a SI could be built up based on the HB-SCF.

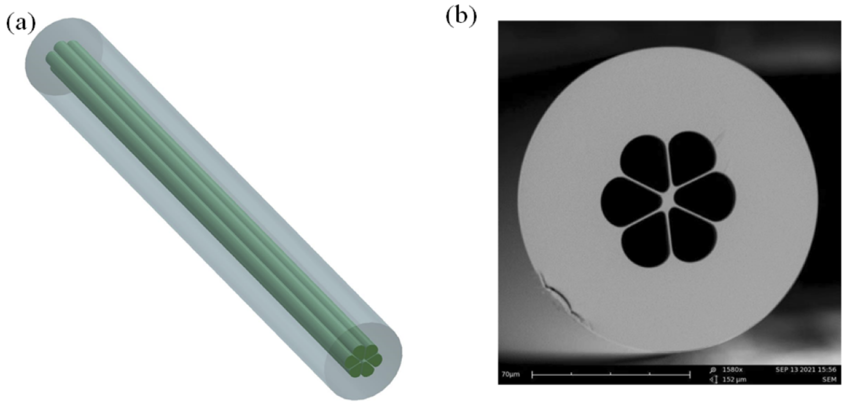

Fig. 1. (a) The structure of the HB-SCF; (b) The cross-section of the HB-SCF under an electron microscope.

Figure 2(a) to (c) shows the fabrication process of the structure of the cascaded interference. The first step is building up a MI based on a 1:1 optical coupler. If the SMF is cut off by the optical fiber cleaver, about 4% of the input light will be reflected and the rest will be dissipated. When the two reflected rays transmit through the coupler, they will be coupled together. The travel length of the reflected light is different if there is a length difference ΔL between the two out fibers, introducing a phase difference. Therefore, a MI is built up, of which the spectrum is shown in Fig. 2(d) by a black line. The free spectral range (FSR) is 0.55 nm.

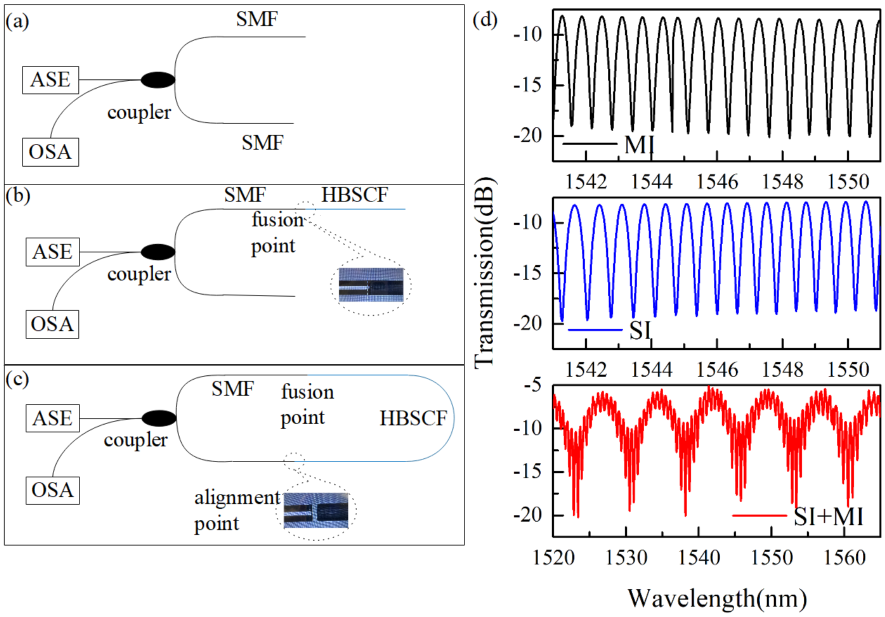

Fig. 2. (a) to (c) The fabrication process of the sensor; (d) the transmitted spectrum at different fabrication processes.

The second step is splicing one of the two output SMFs with the HB-SCF. Manual fusion mode is chosen to avoid collapse introduced by the large air holes in the HB-SCF. Meanwhile, a multiple low power fusion way is used rather than a single high power fusion way to avoid the splicing collapse. The intensity and number of the fusion power are ~300 ms and 10, respectively.The results of the different fusion way are shown in Fig. 3. Using the single high power will cause collapse at the fusion point, resulting in the structure change in the HB-SCF. On the contrary, the boundary between the SMF and the HB-SCF can be easily distinguished when using the multiple low power way to splice the fiber. The blue line in Fig. 2(d) shows the spectrum after the fusion process. The FSR is 0.64nm, which is slightly wider than the FSR before fusion. It can be inferred that the cross-section of the fusion point can also reflect the light but the fusion process has little influence on the FSR of the MI.

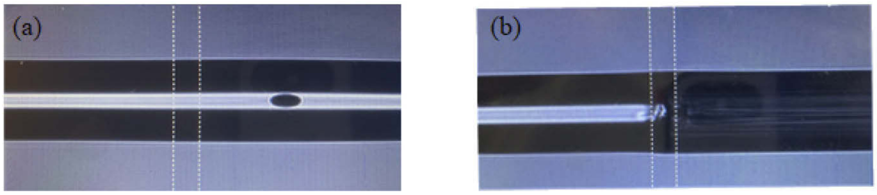

Fig. 3. (a) The fusion result between SMF and HB-SCF under single high-power method; (b) The fusion result between SMF and HB-SCF under multi-low power method.

Concluded from the experiment result, the other output SMF cannot be fused with the HB-SCF because the MI will disappear and only the SI will appear on the final output spectrum. Thus, the last step is aligning the cladding of fiber to build up a SI loop rather than fusing the fiber as the illustration shown in Fig. 2(c). Though there will be a slight gap between the two fibers, it does not influence the sensor function. The alignment of the fiber could also be accomplished by the ceramic ferrule when the sensor works in a more complex environment. The red line in Fig. 2(d) represents the final spectrum. The large FSR interference results from the SI, and the small interference results from the MI. The length of the HB-SCF is 0.68m and the FSR of the MI is 7.3nm. Since the FSR of SI is much large than the MI, the FFT filter could be helpful to distinguish out the different frequencies in the demodulation process.

Generally speaking, at least two optical couplers are needed to achieve the cascade connection of interferometers, which means high insert loss and high system complexity. But the structure we designed is much simpler because just one optical coupler is used.

3. Principles

3.1. Michelson Interference

For the MI, the interference spectrum can be expressed as:

$$I_{MI} = I_1 + I_2 + 2\sqrt{I_1 I_2}\cos(\varphi + \varphi_0) \tag{1}$$

the I_1 and I_2 are the intensity of the reflected light from the out-fiber ends, which are fixed constant. φ_0 is the initial phase difference and φ is the phase difference between the two reflected lights which is related to the length difference$\mathit{\Delta L}$ and the effective index of the fiber core n. Thus, the interference spectrum can also be expressed as:

$$I_{MI} = A_{MI} + B_{MI}\cos(\frac{4\pi n\Delta L}{\lambda} + \varphi_0) \tag{2}$$

where $\mathrm{A_{MI}} = \mathrm{I_1} + \mathrm{I_2}$, $\mathrm{B_{MI}} = (\mathrm{I_1} * \mathrm{I_2})^{1/2}$.

According to the mathematical properties of the cosine function, the I_{MI} reaches its minimum value when φ equals $2(m+1)\pi$ as shown in Eq. (3).

$$\frac{4\pi n\Delta L}{\lambda} = (2m + 1)\pi \tag{3}$$

The FSR is defined as the wavelength difference between the two adjacent interference dips, which can be calculated as:

$$FSR_{MI} = \lambda_2 - \lambda_1 = \frac{\lambda_2\lambda_1}{2n\Delta L} \approx \frac{\lambda^2}{2n\Delta L} \tag{4}$$

When the axial strain of one leg is changed, the$\mathit{\Delta L}$ will extend and increase FSR. However, the relationship between FSR_{MI} and $\mathit{\Delta L}$ is not linear, which. To solve this problem, the A-FFT aiming at a wavelength-domain signal can be applied on the spectrum if the transmitted spectrum is considered a wavelength-domain signal. The definition of the A-FFT in wavelength-domain can be expressed as:

$$F(\omega) = \int_{-\infty}^{+\infty} f(\lambda)e^{-i\omega\lambda}d\lambda \tag{5}$$

The spatial frequency of the spectrum can be obtained through Eq. (5) . The unit of the $F(I_{MI})$ is nm^{-1}, which can also be expressed Hz because the definition of spatial frequency.

According to Eq. (5), Eq. (2) can be transformed as:

$$I_{MI} = A_{MI} + B_{MI}\cos\left(\frac{2\pi\lambda}{FSR_{MI}} + f_0\right) = A_{MI} + B_{MI}\cos(2\pi f_i\lambda + f_0) \tag{6}$$

The A-FFT result of I_{MI} can be calculated as:

$$F(I_{MI}) = C + \frac{B_{MI}}{2}[\delta(f - f_i - f_0) + \delta(f + f_i - f_0)] \tag{7}$$

where C is the constant value and $\delta(f)$ is the impulse function. Therefore, the change of FSR_{MI} can be linearly reflected on the $F(I_{MI})$. Further speaking, the axial strain change of one leg of the MI can be linearly demodulated by the A-FFT method.

3.2. Sagnac interference

For the SI, the interference spectrum can be expressed as:

$$I_{SI} = A_{SI} + B_{SI}\cos\varphi_{SI} \tag{8}$$

The φ_{SI} is the phase difference between the light transmitting through the fast and slow axes, which is related to the length L_B of the HB-SCF and the phase modal birefringence $B(\lambda)$.

$$\varphi_{SI} = \frac{2\pi}{\lambda}BL_B \tag{9}$$

$$B = |n_x^{eff} - n_y^{eff}| \tag{10}$$

The wavelength of interference dip can be expressed as:

$$\lambda = \frac{2BL_B}{2m+1} \tag{11}$$

If the length variation caused by lateral stress is ignored, the relationship between wavelength shift and lateral stress can be deduced as:

$$\frac{d\lambda}{dP} = \frac{2L_B}{2m+1}\frac{dB}{dP} \tag{12}$$

The orange line in Fig. 4(a) is the transmitted spectrum obtained during the experiment. The blue line is the result curve of the low pass FFT filter below 0.17 Hz. The SI spectrum can

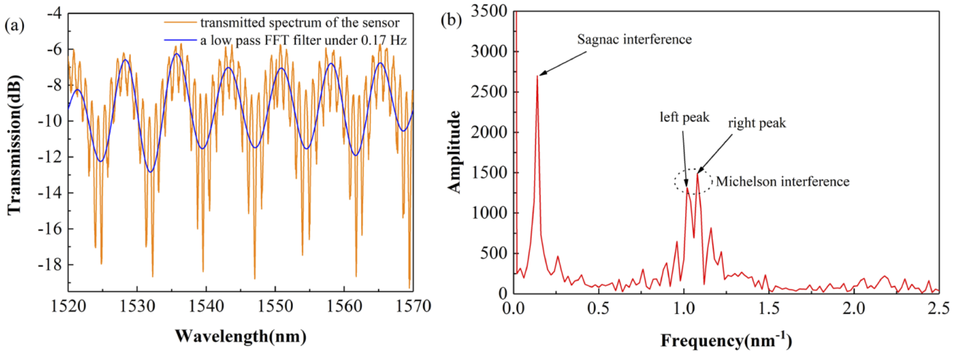

Fig. 4. (a) The final output spectrum of the sensor and the low pass FFT filter result; (b) The A-FFT result of the sensor spectrum.

be reproduced as expected because 0.17 Hz is slightly bigger than the spatial frequency of SI. Figure 4(b) is the A-FFT result curve of the sensor spectrum. The low-frequency peak is introduced by the SI while the high-frequency peak is introduced by the MI. There are two peaks introduced by the MI which is consistent with Eq. (7). Theoretically, the sensitivities of the two peaks should be the same.

4. Experimental Results

4.1. Lateral stress sensing experiment

The light is input by an ASE laser of which the spectrum region is from 1500 nm to 1600nm. The transmitted spectrum is obtained by an optical spectrum analyzer (OSA, AQ6070D) of which the minimum resolution is 0.02 nm. About 25 cm HB-SCF is coiled and stuck to a horizontal platform as shown in Fig. 5. Then an acrylic plate is put on the fiber to ensure the even distribution of pressure. When the standard weight objects amount is increased or decreased, the lateral stress applied on HB-SCF is also changed. The weight of the single standard weight object is 0.5 kg and the size of the acrylic plate is 25cm×10cm. Thus, the intensity of pressure exerted on the fiber by every weight is 200 Pa.

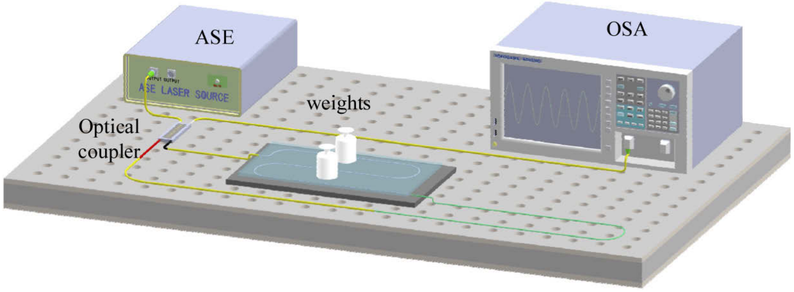

Fig. 5. The experiment system for lateral stress sensing.

According to the analysis result in chapter 2.2, the interference dip wavelength of SI will shift with the change of the lateral stress. A low-pass FFT filter whose threshold is 0.17 Hz is applied to obtain the spectrum of SI. The different color lines in Fig. 6(a) represent the FFT filter result under different lateral stress from 0 Pa to 1200 Pa. The spectrum shifts to the long-wavelength with the increasing of the lateral stress. Figure 6(b) shows the linear fitting between the pressure intensity and the interference dip wavelength at about 1540 nm. The slope of the fitting curve stands for the sensitivity of wavelength with the lateral stress changes, which is 3.13 pm/Pa (also expressed as 3.13 nm/kPa). The degree of fitting R^2 is 0.99034, which signifies that the sensor responds linearly to the lateral stress change. Thus, the maximum lateral stress P_M the sensor can detect will be calculated by: $\mathrm{P_M = FSR_{SI}/S_{pa}} = 7.3$ nm/(3.13 pm/Pa) =2332 Pa. The minimum lateral stress P_m the sensor can detect relates with resolution the OSA which is 0.02 nm. Upon that, the P_m can be calculated as 0.02 nm/(3.13 pm/Pa) =6.39 Pa.

Figure 6(a) displays the FFT curve of the original spectrum under different lateral stress. What can be extracted is that the lateral stress does not influence the frequency of MI and SI.

4.2. Axial strain sensing experiment

Similar to the lateral stress sensing experiment, the light source is also an ASE, and spectrum record equipment is also OSA. The axial strain sensing is completed by the MI part. One leg of the MI is fixed horizontally on the three-dimensional adjustment frame by fiber clamps as shown

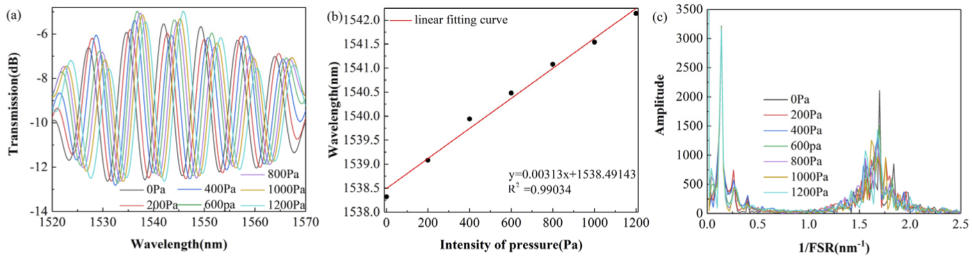

Fig. 6. (a) The transmitted spectrum under different lateral stress after 0.17 Hz low pass FFT filter; (b) The linear fitting curve between the dip wavelength at ~1540 nm and lateral stress; (c) The A-FFT result of the transmitted spectrum under different lateral stress.

in Fig. 7. The distance between the two three-dimensional adjustment frames is 20 cm and the space can be adjusted by the micrometer. The minimum adjustment step of the micrometer is 0.01 mm and the minimum axial strain provided by every adjustment step is 0.01 mm/20cm = 50 με.

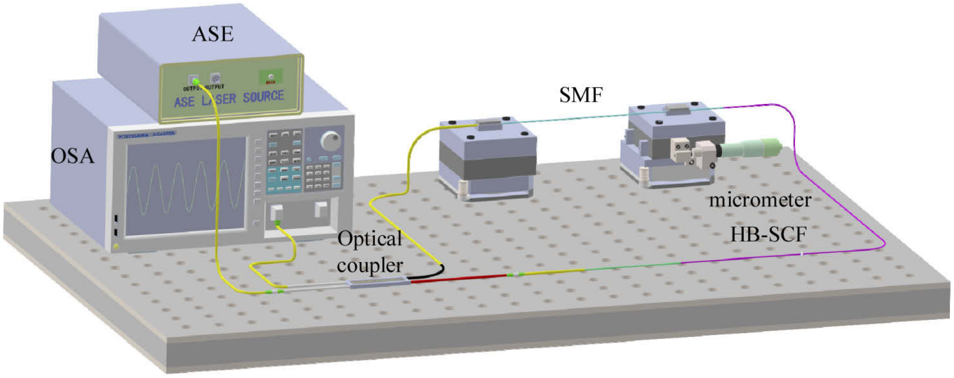

Fig. 7. The experiment system for axial strain sensing.

Figure 8(a)is the result of a low-pass FFT filter under 0.17 Hz at different axial strains from 0 to 4000 με. The spectrum has no wavelength shift because only the axial strain of the MI is changed. The A-FFT result of the sensor spectrum is drawn in Fig. 8(b). With the increase of the axial strain, the frequency of the MI gradually shifts to the low frequency which indicates that the FSR of MI becomes larger. The right peak of the MI FFT curve is chosen as the observation point. Figure 8(c)is the linear fitting between the frequency of MI and the axial strain. The sensitivity of the MI frequency to the change of axial strain is $1.846e^{-4}$ $(\text{nm}\cdot\mu\varepsilon)^{-1}$ and the degree of fitting R^2 is *0.98853*. The minimum interval of the A-FFT result is 0.02 nm^{-1} and then the minimum axial strain S_m the sensor can detect is $S_m = (0.02\ \text{nm}^{-1})/[1.846e^{-4}\ (\text{nm}\cdot\mu\varepsilon)^{-1}] = 108.34\mu\varepsilon$.

4.3. Simultaneous measurement of lateral stress and axial strain

According to the above discussion, the MI part of the sensor is sensitive to the axial strain but insensitive to the lateral stress, while the SI part is sensitive to the lateral stress but insensitive to the axial strain. It implies that the cascaded interference sensor could simultaneously measure axial strain and lateral stress without cross-sensitivity. The dual-parameters sensing system is built up to verify this hypothesis, as shown in Fig. 9. One leg of the MI is horizontally fixed on the three-dimensional adjustment frame by fiber clamps and a length of HB-SCF is put between

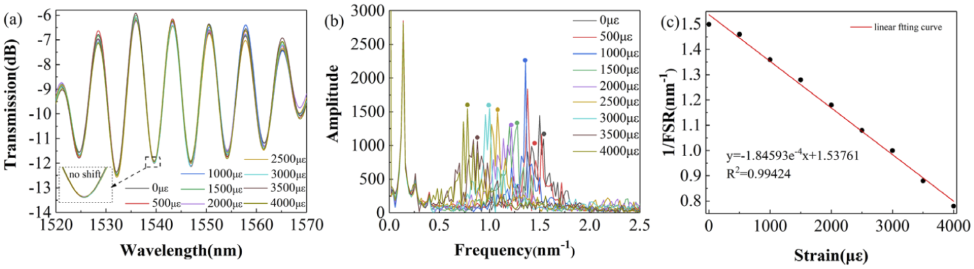

Fig. 8. (a) The transmitted spectrum under different axial strain after 0.17 Hz low pass FFT filter; (b) The A-FFT result of the transmitted spectrum under different axial strain; (c) The linear fitting curve between the frequency of MI and axial strain.

the platform and the acrylic plate. Then by adjusting the distance between the two fiber clamps and changing the number of the weight on the acrylic plate at the same time to achieve the simultaneous change of axial strain and lateral stress. According to the resolution of the OSA, the allowable range of measurement errors for axial strain and lateral stress are ±108.34 με and ±6.39 Pa, respectively.

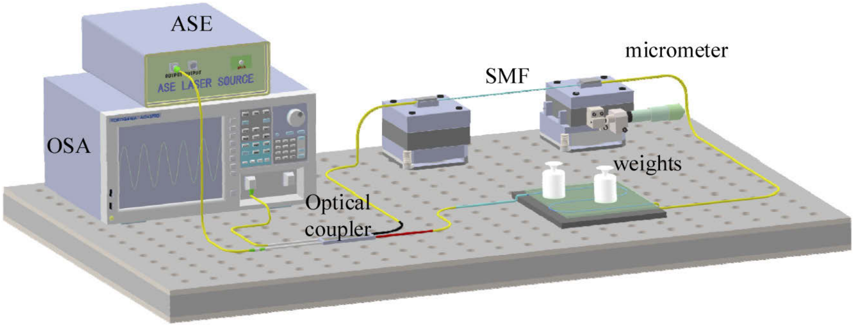

Fig. 9. The experiment system for measuring the lateral stress and axial strain.

Two experiments were conducted based on this system. The first one is that change the axial strain of the MI just one time but change the lateral stress in the range from 0 to 1000 Pa. The result is shown in Fig. 10. The black line in the picture represents the initial state of the sensor without any axial strain and lateral stress change and the red line is the output spectrum after changing the axial strain of MI. The other color line is the transmitted spectrum under different lateral stress. The change value of the axial strain can be calculated by the offset between the A-FFT result black and red lines while the change value of the lateral stress can be calculated by the same method in chapter 4.1. Figure 10(c) is the comparison result between the experimental value and the standard value. The standard value of the axial strain change is 1250 με and the standard lateral stress change interval is 200 Pa. There are two points out of the error range and the correct rate for simultaneous measurement is 66.67%.

Another experiment is changing the lateral stress of the SI just one time but changing the axial strain in a wide range from 0 to 3000 με. The result is shown in Fig. 11 and the correct rate is 57.14% within the error range allowed. The two primary error sources are system error and sensor error. The system error is primarily related to the resolution of the OSA. Improving the resolution of the OSA can help reduce system error. The error induced by the sensor itself could be eliminated by increasing the linearity of the sensor response which may be related to the sensor fabrication process.

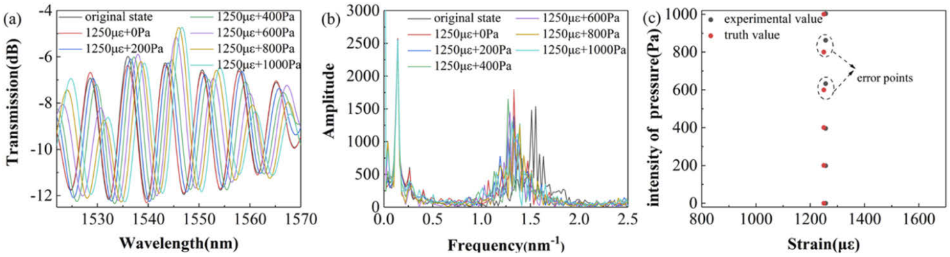

Fig. 10. (a) The transmitted spectrum of dual-parameters sensing experiment after 0.17 Hz low pass FFT filter; (b) The A-FFT result of the transmitted spectrum of dual-parameters sensing experiment; (c) The comparison between the demodulation value and the actual value.

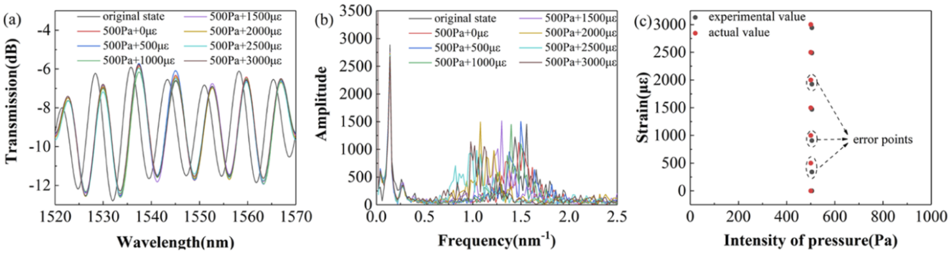

Fig. 11. (a) The transmitted spectrum of dual-parameters sensing experiment after 0.17 Hz low pass FFT filter; (b) The A-FFT result of the transmitted spectrum of dual-parameters sensing experiment; (c) The comparison between the demodulation value and the actual value.

Thus, the proposed sensor is capable of measuring the axial strain and lateral stress simultaneously. The measurement ranges are 0 to 3000 με and 0 to 1000 Pa, respectively.

5. Discussion

The sensor published in Ref. [23] is a cascaded interferometer structure between MZI and SI, which is also designed for simultaneous measurement of axial strain and lateral stress. However, this sensor has cross-sensitivity between axial strain and lateral stress, resulting in the dual-parameter sensing experiment only staying in the stage of theoretical analysis. By contrast, the proposed sensor has no cross-sensitivity and the accuracy rate for simultaneous measurement is 66.67%. In addition, it is easy to find that the proposed sensor is more sensitive to lateral stress than other sensor structures from Table 1 below. Thus the proposed sensor has great potential

Table 1. The sensing performance of other sensors

Structure	Strain Sensitivity	Lateral stress Sensitivity	Dual-parameters sensing	Cross sensitivity	Reference
DPMZI-SI	5.65 pm/με	1.28 nm/kPa	-	high	[23]
MI-PMF	-	1.93 nm/kPa	-	-	[24]
PFBG	-	1.3 nm/kPa	-	-	[25]
SI-PMF	-	1.746 pm/kPa	-	-	[26]
SI-MI	$1.846e^{-4}/(nm\cdot\mu\varepsilon)$	3.13 nm/kPa	66.67%	0	This work

application in many sensing systems, such as the health monitoring system for paralyzed, the using status of safety belt monitoring system in the car seat, and so on.

6. Conclusions

In summary, a dual-parameter sensor for simultaneous measurement of axial strain and lateral stress is proposed. The main part of the sensor is a cascaded interferometer structure which consists of a MI and a SI. The common single high power fusion way is replaced by the multi low power fusion way to obtain this structure. With the help of the A-FFT and FFT filter, the sensor responds linearly to the axial strain and lateral stress change. The axial strain sensitivity is $1.846e^{-4}$ $(\mathrm{nm}\cdot\mu\varepsilon)^{-1}$and the lateral stress sensitivity is 3.13 pm/Pa. Since there is no cross-sensitivity between the two sensing parts, the sensor could be used for dual-parameter sensing applications. Experimental result demonstrates that the sensor can detect the variation of axial strain and lateral stress at the same time within the range of errors permitted.

Funding. Shenzhen-HK-Macao Science and Technology Plan C Grant (SGDX2020110309520303); National Natural Science Foundation of China (61905096, 61975250); Guangdong Provincial Pearl River Talents Program (2017BT01X121); Research Grants Council, University Grants Committee (GRF15211317).

Acknowledgments. The high-birefringence suspended core fiber used in this paper was designed and fabricated by Zhengyong Liu.

Disclosures. The authors declare no conflicts of interest.

Data availability. Data underlying the results presented in this paper are not publicly available at this time but may be obtained from the authors upon reasonable request.

References

1. T. K. Yadav, R. Narayanaswamy, M. H. Abu Bakar, Y. M. Kamil, and M. A. Mahdi, "Single-mode tapered fiber-optic interferometer based refractive index sensor and its application to protein sensing," Opt. Express **22**(19), 22802–22807 (2014).
2. L. Li, L. Xia, Z. Xie, and D. Liu, "All-fiber Mach-Zehnder interferometers for sensing applications," Opt. Express **20**(10), 11109–11120 (2012).
3. C. Tao, H. Wei, and W. Feng, "Photonic crystal fiber in-line Mach-Zehnder interferometer for explosive detection," Opt. Express **24**(3), 2806–2817 (2016).
4. Z. B. Liu, Z. Tan, B. Yin, Y. Bai, and S. Jian, "Refractive index sensing characterization of a singlemode-claddingless-singlemode fiber structure based fiber ring cavity laser," Opt. Express **22**(5), 5037–5042 (2014).
5. A. Masoudi and T. P. Newson, "High spatial resolution distributed optical fiber dynamic strain sensor with enhanced frequency and strain resolution," Opt. Lett. **42**(2), 290–293 (2017).
6. X. Hong, J. Wu, C. Zuo, F. Liu, H. Guo, and K. Xu, "Dual Michelson interferometers for distributed vibration detection," Appl. Opt. **50**(22), 4333–4338 (2011).
7. C. Wang, Y. Shang, X. H. Liu, C. Wang, H. H. Yu, D. S. Jiang, and G. D. Peng, "Distributed otdrinterferometric sensing network with identical ultra-weak fiber bragg gratings," Opt. Express **23**(22), 29038–29046 (2015).
8. K. Hotate and K. Kajiwara, "Proposal and experimental verification of Bragg wavelength distribution measurement within a long-length FBG by synthesis of optical coherence function," Opt. Express **16**(11), 7881–7887 (2008).
9. J. Zhou, C. Liao, Y. Wang, G. Yin, X. Zhong, K. Yang, B. Sun, G. Wang, and Z. Li, "Simultaneous measurement of strain and temperature by employing fiber Mach-Zehnder interferometer," Opt. Express **22**(2), 1680–1686 (2014).
10. X. Zhao, M. Dong, Y. Zhang, F. Luo, and L. Zhu, "Simultaneous measurement of strain, temperature and refractive index based on a fiber Bragg grating and an in-line Mach-Zehnder interferometer," Opt. Commun. **435**, 61–67 (2019).
11. Y. J. Rao, X. K. Zeng, Y. P. Wang, T. Zhu, Z. L. Ran, L. Zhang, and I. Benning, "Temperature-strain discrimination using a wavelength-division-multiplexed chirped in-fiber-Bragg-Grating/extrinsic Fabry-Perot sensor system," Chin. Phys. Lett. **18**(5), 643–645 (2001).
12. M.-S. Yoon, S. Park, and Y.-G. Han, "Simultaneous measurement of strain and temperature by using a micro-tapered fiber grating," J. Lightwave Technol. **30**(8), 1156–1160 (2012).
13. P. Lu, L. Men, K. Sooley, and Q. Chen, "Tapered fiber Mach-Zehnder interferometer for simultaneous measurement of refractive index and temperature," Appl. Phys. Lett. **94**(13), 131110 (2009).
14. P. Lu and Q. Chen, "Asymmetrical Fiber Mach-Zehnder Interferometer for Simultaneous Measurement of Axial Strain and Temperature," IEEE Photonics J. **2**(6), 942–953 (2010).
15. Y. Li, P. Lu, Z. Qu, W. Zhang, W. Ni, D. Liu, and J. Zhang, "An Optical Fiber Twist Sensor With Temperature Compensation Mechanism Based on T-SMS Structure," IEEE Photonics J. **12**(1), 1–8 (2020).

16. J. Wang, L. Pei, J. Wang, Z. Ruan, J. Zheng, J. Li, and T. Ning, “Magnetic field and temperature dual-parameter sensor based on magnetic fluid materials filled photonic crystal fiber,” Opt. Express **28**(2), 1456–1471 (2020).
17. B. Gu, W. Yuan, S. He, and O. Bang, “Temperature Compensated Strain Sensor Based on Cascaded Sagnac Interferometers and All-Solid Birefringent Hybrid Photonic Crystal Fibers,” IEEE Sens. J. **12**(6), 1641–1646 (2012).
18. L. Chen, W. G. Zhang, Y. J. Liu, L. Wang, J. Sieg, and B. Wang, “Real time and simultaneous measurement of displacement and temperature using fiber loop with polymer coating and fiber Bragg grating,” Rev. Sci. Instrum. **85**(7), 075002 (2014).
19. C. Sun, M. Wang, Y. Dong, S. Ye, and S. Jian, “Simultaneous measurement of magnetic field and temperature based on NCF cascaded with ECSF in fiber loop mirror,” Opt. Fiber Technol. **48**, 45–49 (2019).
20. Y. Miao, H. Zhang, J. Lin, B. Song, K. Zhang, W. Lin, B. Liu, and J. Yao, “Simultaneous measurement of temperature and magnetic field based on a long period grating concatenated with multimode fiber,” Appl. Phys. Lett. **106**(13), 132410 (2015).
21. L. Wang, W. G. Zhang, P. C. Geng, S. C. Gao, J. L. Li, Z. Y. Bai, and L. Chen, “Simultaneous directional bending and temperature measurement with overlapping long period grating and fiber Bragg grating structure,” J. Opt. **16**(5), 055401 (2014).
22. Z. Liu, C. Wu, M. Vincent Tse, and H. Tam, “Fabrication, Characterization, and Sensing Applications of a High-Birefringence Suspended-Core Fiber,” J. Lightwave Technol. **32**(11), 2113–2122 (2014).
23. S. Wang, P. Lu, L. Mao, D. Liu, and S. Jiang, “Cascaded interferometers structure based on dual-pass Mach–Zehnder interferometer and Sagnac interferometer for dual-parameter sensing,” Opt. Express **23**(2), 674–680 (2015).
24. J. Yuan, K. Zhang, W. Yao, B. Liu, Q. Li, Z. Zhang, K. Zhang, R. Chen, and S. Wang, “A simple fiber lateral stress sensor based on polarization-maintaining fiber embedded Michelson interferometer assisted by silicon rubber sheets,” Optik **203**, 164008 (2020).
25. Z. F. Zhang, X. M. Tao, H. P. Zhang, and B. Zhu, “Soft Fiber Optic Sensors for Precision Measurement of Shear Stress and Pressure,” IEEE Sens. J. **13**(5), 1478–1482 (2013).
26. Y. H. Yuan, J. Li, W. Q. Duan, X. Zhang, W. Jin, and M. W. Yang, “An embedded pressure sensor based on polarization maintaining photonic crystal fiber,” Meas. Sci. Technol. **24**(9), 094004 (2013).